

# Nanostructure and microstructure of laser-interference induced dynamic patterning of Co on Si

L.Longstreth-Spoor, J.Trice, \*H.Garcia, C.Zhang, and Ramki Kalyanaraman\*

Department of Physics, Washington University in St. Louis, MO 63130

Center for Materials Innovation, Washington University in St. Louis, Mo 63130

\*Department of Physics, Southern Illinois University, Edwardsville, IL 62026

## Abstract

We have investigated the nanostructure and microstructure resulting from ns laser irradiation simultaneous with deposition of Co films on Si(001) substrates. The spatial order and length scales of the resulting nanopatterns and their crystalline microstructure were investigated as a function of film thickness  $h$  and laser energy density  $E$  using a combination of atomic force, scanning electron and transmission electron microscopies. The results could be classified into two distinct categories based on the laser energy density used. It was observed that the thickness-dependent  $E$  required to melt the Co film ( $E_{Co}$ ) was lower than Si ( $E_{Si}$ ) primarily because of the higher reflectivity of Si. Consequently, for energy densities  $E_{Co} < E_1 < E_{Si}$  that preferentially melted the Co film, spatially ordered nanoparticles were formed and were attributed to capillary-driven transport in the liquid phase. The ordering length scale corresponded to the interference fringe spacing  $\Lambda$  and the microstructure was primarily Co metal and a metal-rich silicide phase. The native oxide layer played an important role in minimizing the Co-Si reaction. For laser energy densities  $E_2 \geq E_{Si}$ , spatially ordered patterns with periodic length scales  $L < \Lambda$  were observed and resulted from interference of an incident laser beam with a beam transmitted into the Si substrate. These nanopatterns showed one- as well as two-dimensional spatial ordering of the nanostructures. The microstructure in this laser energy regime was dominated by silicide formation. These results suggest that various nanostructures and microstructures, ranging from nearly pure metal to a Si-rich silicide phase can be formed by appropriate choice of the laser energy simultaneous with film growth.

---

\*ramkik@wuphys.wustl.edu

## 1 Introduction

Metal and metallic compounds with nanometer scale (1-1000 nm) features arranged in spatially ordered geometries offer various functionalities [1, 2], including: in regular arrays of discrete nm scale magnets for potential memory storage devices [3, 4]; surface plasmon waveguides made from linear chains of metal nanoclusters [5, 6]; and as spatially ordered metal nanocatalyst seeds to make high-efficiency flat-panel displays from carbon-nanotube arrays [7]. In these applications, the control of ordering, including spatial arrangement of the nanofeatures, control of its size, shape, composition, and crystallographic orientation is important. In most instances, the ability to control ordering over large length scales, i.e. to have long-range ordering, is also necessary [8]. In this regard, laser-based patterning of surfaces of metals, semiconductors and insulators is a promising approach. The area of laser-surface interactions has been broadly explored in the past for a fundamental understanding of pattern forming processes and towards applications requiring ordered surface structures [9, 10]. One area is that of laser-induced chemical vapor deposition [11] while the other is direct irradiation of surfaces leading to rippling and pattern formation due to various mechanisms, including interference between incident and scattered light waves [12, 13], thermocapillary flow [14] and other instabilities [15]. This pattern forming approach has been used in various applications, including grating creation [16] and quantum dot arrays [17]. Recently, the group of Pedraza et al. [18, 19] showed how spatially ordered nanostructures could be formed in controlled ways by irradiation of the Si surface with ns laser pulses. The patterning process was a result of deformation of the surface via thermocapillary effects, while the length scales observed in the patterning also included those arising from interference of the incident light with scattered waves.

Another interesting area of pattern formation is when laser light interacts through optical and/or thermal effects with a time-varying system, such as found in the deposition of thin films. During the early stages of film growth from the vapor phase, the surface morphology changes dramatically due to nucleation and growth processes. These processes are in turn critical functions of experimental parameters like deposition rate, surface temperature and the presence of surface defects. In this respect, a large body of work has been performed on developing strategies to create thin film structures with homogeneous properties over large areas, for example having uniformity in thickness, crystal structure, grain orientation, etc. in the plane of the substrate [20]. On the other hand, recent interest in creating large-area structure having spatially ordered inhomogeneities on the nm length scale have spurred new experiments to modify film nucleation and growth. One example is the recent work of Timp and co-workers [21, 22] and McClelland and co-workers [23] who used a laser-interference pattern to modify atom beams such that the flux of depositing film material was spatially periodic on the substrate surface. Consequently, nm scale periodic patterns were generated.

Recently we investigated the role of thermal effects arising from laser-interference irradiation performed simultaneously with metal film deposition. We showed in these experiments that when the growing film/substrate surface is simultaneously irradiated with ns pulsed laser interference patterns, long-range ordered morphologies can be achieved [24, 25]. In those experiments, a 9 ns pulsed laser operating at 50 Hz with energy density  $\leq 20 \text{ mJ/cm}^2$  were used to dynamically pattern the films and the mechanism was attributed primarily to surface diffusion of the metal atoms under the transient temperature gradients created on the substrate surface. However, since the temperature transients only lasted for times of the order of 10

ns [26] which was very small compared to the time between pulses of 20 ms, the observed patterning was weak, as evidenced by the diffuse lines with small aspect ratio [25]. Many nanoscale applications require well defined surface structures such as wires and particles which have aspect ratios of  $O(1)$ . We recently observed that when dynamic patterning is performed under laser energy densities that are sufficient to melt the metal film, then features with larger aspect ratios can be achieved [27].

In this work we present detailed experimental results of dynamic patterning of nanoscopic Co on Si(001) as a function of film thickness and laser energy in regimes dominated by melting. The patterning was performed using two-beam interference irradiation with a 9 ns, 266 nm pulsed laser operating at 50 Hz. The resulting nanostructure and microstructure were characterized using atomic force microscopy (AFM), secondary electron microscopy (SEM) and transmission electron microscopy (TEM). We determined that the laser melt threshold  $E_m$  for the bare Si surface was larger than for Co films,  $E_{Co}$ , primarily due to the difference in reflectivities. Also,  $E_{Co}$  increased as the film thickness decreased due to the enhanced heat sinking by the substrate. As a result of this, the patterning results could be classified into two categories: (i) For patterning in regime  $E_{Co} < E_1 < E_{Si}$ , the patterns showed a length scale consistent with the interference fringe spacing  $\Lambda$  and the microstructure was primarily Co metal and/or a Co-rich phase. The pattern mechanism in this regime was attributed primarily to capillary flow in the liquid phase based on an estimate of the time scale and flux; (ii) The patterning in regime  $E_2 \geq E_{Si}$  was dictated primarily by the rippling of the Si surface with the ordering length scales having spacing  $L < \Lambda$  because of interference between an incident beam and a transmitted electromagnetic wave in Si. The microstructure in this regime was dominated by silicide formation. These results show that a wide variety of nanostructures and microstructures can be obtained by choice of laser energy and film thickness.

## 2 Experiment

Co films ranging from 0.5 nm to 10 nm in thickness were deposited by e-beam evaporation onto p-type Float-zone Si(001) substrates with resistivity of  $65 - 80 \Omega - cm$ . E-beam evaporation of Co was performed at room temperature in ultrahigh vacuum (base P of  $2 \times 10^{-8}$  Torr) at deposition rates between 0.1 to 1 nm/min. A *TECTRA* e-flux mini e-beam evaporator was used for this purpose. The evaporation and laser irradiation geometry is shown in Fig. 1. *In-situ* thickness measurements were made using an *Inficon* Model XTM/2P quartz crystal thickness monitor. Roughness measurements were made of the deposited films using the AFM. The measurements showed that average peak-to-peak roughness was less than 0.2 nm for the range of thickness studied and virtually independent of the deposition rate. The deposition chamber, laser and necessary laser optics were mounted on a custom-built mechanical isolation table with I-2000 isolation legs from Newport. The vacuum pumping was achieved by a combination of an *Osaka* Magnetically levitated turbomolecular pump model TH260MCA and *Physical Electronics* TiTan 400L Ion pump. The backing pump was a *Leybold* ECODY-L oil-free pump located in an adjacent room to minimize vibration effects. The Si(001) substrates were degreased in methanol, acetone and DI water prior to insertion into the chamber. We observed that the removal of the native oxide layer enhanced formation of reacted microstructures and hence no attempt was made to etch the oxide for the results presented here.

For the laser interference we used a *Spectra Physics* Injection seeded Lab-130-50 Nd:YAG laser operating at its 4<sup>th</sup> harmonic of 266 nm, with a temporal FWHM of  $\tau_p \sim 9$  ns, repetition rate  $f = 50$  Hz and spatial coherence length  $> 2$  m to perform two-beam laser interference irradiation. The unfocused output of the laser has a multi-mode profile with linear polarization and an area of  $1\text{ cm}^2$  with an energy distribution that corresponded to a  $\sim 70\%$  Gaussian fit. The maximum total energy per pulse was approximately 44 mJ. For this experiment, the pattern formation reported was for regions of the beam in which the energy variation was  $\leq 15\%$ . Two-beam laser interference was performed using two p-polarized beams obtained by splitting the original beam using a 50-50% beamsplitter. The energy of each beam was measured using an *Ophir* optronics 30A-P thermopile head and the *Nova* power meter. For the interference, beam 1 was incident on the substrate at  $45^\circ$  incidence while beam 2 was rotated by an angle of between  $38^\circ - 45^\circ$  from beam 1, as depicted in Fig. 1. To maximize the interference intensity contrast, the individual beam energy densities were controlled by lenses. The primary asymmetry in the energy of two beams interfering on the surface came from the higher reflectivity and the larger projected area for beam 2. This was partially compensated by focusing the beams using a 500 mm lens in the path of the off-normal beam and a 750 mm lens for the  $90^\circ$  beam. We estimated that the experimental fringe contrast was between 80 – 90%. The energy density of *each* beam after focusing was in the range of  $50\text{-}200\text{ mJ/cm}^2$  for energy regime  $E_1$  and  $200\text{--}250\text{ mJ/cm}^2$  for regime  $E_2$ . The results presented in this work were from an approximately  $25\text{ }\mu\text{m} \times 25\text{ }\mu\text{m}$  wide region of interference on the samples. The interference angle  $2\theta$  between the beams varied between  $38^\circ - 45^\circ$  for the pair of vacuum ports chosen in this work. The resulting interference length scale on the surface was  $\Lambda = \frac{\lambda}{2S\sin 2\theta}$ , where  $\lambda = 266\text{ nm}$  is the incident wavelength.

Following the deposition and irradiation, both done in vacuum, the samples were removed for characterization. The nanostructures were characterized using contact-mode atomic force microscopy (AFM) and/or Scanning electron microscopy (SEM). AFM was performed in ambient conditions using a *Molecular Imaging* PicoScan AFM with a BudgetSensors AFM tip of spring constant 0.2 N/m. The measured lateral ( $x - y$ ) resolution was  $\sim 10$  nm and  $z$ -height resolution was  $\sim 0.2$  nm. SEM was performed using a Hitachi S-4500 microscope. The microstructure was studied in the TEM using plan-view geometry and a 200 keV JEOL 2000FX microscope. The plan-view TEM samples were prepared using a well-known Si etching procedure. The Si substrate was mechanically ground until it was reduced to 100 micron thickness. Next an etchant of hydrofluoric acid, nitric acid and acetic acid in a 5:2:2 ratio was used to etch through the back of the Si substrate till a hole was visible at which point the sample was sufficiently thin to allow for TEM analysis.

### 3 Results and Discussion

We observed that the overall results on the nature of spatial ordering, resulting surface morphology and microstructure could be separated into three distinct categories based on the laser energy used. One category belonged to the regime when the laser energy density was above the critical laser energy density  $E_{Si}$  of  $\sim 200\text{ mJ/cm}^2$ . For all  $E \geq E_{Si}$  we observed that the bare Si surface underwent rippling under otherwise identical conditions of interference. It has been shown earlier by Pedraza and co-workers that this surface rippling occurs when the energy absorbed is sufficient to melt the Si surface [18, 19]. Therefore the energy

$E_{Si}$  was taken as the melt threshold for the Si surface under the experimental conditions used in this work. Another category of results corresponded to energies  $50 \leq E_1 < 200$  where Si rippling could not be observed and the resulting Co morphology consisted of well-defined nanostructures with clear evidence of a droplet microstructure. The lower energy identified as  $E_{Co}$ , was the lower bound on the threshold of melting of Co during the dynamic patterning. The final category of surface structures observed has been detailed by us in earlier publications and consisted primarily of diffuse morphologies at energies  $E < E_{Co}$  [24, 25]. Below we detail the results obtained in the two energy regimes  $E_1$  and  $E_2$ . First we begin by showing that the melt threshold energy for Co on Si is always smaller than the Si melt threshold consequent to which the mechanism of pattern formation in the various regimes may be identified.

### 3.1 Estimate of melt threshold vs. Co film thickness and lateral temperature gradient

In the experimental results presented in Sec. 3.2 we observed two important results: (i) the Co film appeared to melt at energies lower than the Si substrate despite the higher melting point of Co; and (ii) ordered patterns with length scales corresponding to the laser interference fringe spacing were formed. To understand these two effects we performed analytical and finite element calculations of heating by laser irradiation. We have recently derived an analytic and numerical solution for heating of nanoscopic metal films by a spatially uniform pulsed laser on transparent and absorbing substrates [26]. Excellent agreement between the solution and experiment was found in predicting the threshold energy density needed to melt nanoscopic Co films (with thickness less than the laser absorption depth  $\alpha^{-1} \sim 11\text{ nm}$ ) on  $\text{SiO}_2$  substrates. One of the important results obtained by us was that the laser energy required to melt the film increased as the film thickness decreased for metal films on *insulating* substrates [28]. Here, the experiments were performed primarily on thermally conducting Si substrates. To determine the trend in energy vs film thickness, we computed the laser energy required to achieve a temperature rise of the Co metal film to the melting temperature of Si of 1683 K by a uniform laser intensity distribution. In this way complications of phase change could be avoided. Fig. 2 shows the geometry of the film-substrate system used in the thermal modeling. The previously determined solution for the local film heating was as follows [26]:

$$T(t) = T_o + A - B \quad (1)$$

where:

$$A = \frac{2}{\sqrt{\pi}} \cdot \left( \frac{S_1}{K} + \frac{S_2}{a_s \sqrt{\alpha_s}} \right) \sqrt{t} + \frac{S_1}{K^2} \cdot \left( e^{K^2 t} \cdot \text{erfc}(K \sqrt{t}) - 1 \right)$$

$$B = \frac{S_2}{a_s^2 \alpha_s K} \cdot \left( K + a_s \sqrt{\alpha_s} + \frac{K^2 \cdot e^{a_s^2 \alpha_s t} \text{erfc}(a_s \sqrt{\alpha_s t})}{a_s \sqrt{\alpha_s} - K} - \frac{a_s^2 \alpha_s e^{K^2 t} \text{erfc}(K \sqrt{t})}{a_s \sqrt{\alpha_s} - K} \right)$$

$S_1$  and  $S_2$  are defined via

$$S_1 = \frac{(1 - R(h))}{(\rho C_p)_m h} \cdot \frac{E}{t_p} \cdot (1 - \exp(-a_m h)) \quad (2)$$

$$S_2 = \frac{(1 - R(h)) \cdot a_s}{(\rho C_p)_s} \cdot \frac{E}{t_p} \quad (3)$$

$\alpha_s$  is expressed as

$$\alpha_s = \frac{k_s}{(\rho C_p)_s} \quad (4)$$

and  $K$  is given by

$$K = \frac{\sqrt{(\rho C_p k)_s}}{(\rho C_p)_m h} \quad (5)$$

Here  $T_o$  corresponds to room temperature;  $R(h)$  is the effective film-thickness dependant reflectivity for the Co/Si system as proposed by Ref. [29]. A plot of  $R$  versus  $h$  is presented in Fig. 3(a) for the Co-Si system;  $E_o$  is the laser energy density;  $a$  is the material absorption coefficient;  $\rho$  is the density;  $C_p$  is the specific heat;  $h$  is the Co film thickness;  $t_p$  is the laser pulse width; and  $k$  is the thermal conductivity. The subscripts “m” and “s” denote the metal and the substrate respectively. In Fig. 3(b), the predicted trend in the needed threshold energy density to heat the Co film to the Si melting point is presented. Since our experiments primarily involved two-beam interference, we have presented the figure in terms of the energy density of an individual beam with the assumption of identical energy in the second beam and therefore a resulting fringe contrast of 100%. As the figure shows, the energy required to melt a continuous Co film increases with decreasing film thickness. This trend arises because for two primary reasons: (i) the increasing reflectivity of the Co/Si system as a function of decreasing film thickness; and (ii) the increasing role of the Si substrate as a heat sink. Based on this calculation, our experimental observations, to be discussed in sec. 3.2 and 3.3, appear to be consistent with patterning in regime  $E_1$  arising from preferential melting of Co and in  $E_2$  due to the melting of Si respectively. The second calculation made by us was an estimate of the lateral temperature gradient along the plane of the film arising from the laser interference pattern. We used the finite element method via the commercial code FlexPDE. The model solved the two-dimensional heat equation in the film and substrate domains. The heat equation in the film domain was given by:

$$\frac{\partial T(x, y, t)}{\partial t} = \frac{k_m}{(\rho C_p)_m} \left( \frac{\partial^2}{\partial x^2} T(x, y, t) + \frac{\partial^2}{\partial y^2} T(x, y, t) \right) + 4 \cdot S'_1 \cos\left(\frac{2\pi x}{F}\right) \cdot \exp(-a_m \cdot y) \quad (6)$$

and in the substrate domain

$$\frac{\partial T_s(x, y', t)}{\partial t} = \frac{k_s}{(\rho C_p)_s} \left( \frac{\partial^2}{\partial x^2} T_s(x, y', t) + \frac{\partial^2}{\partial y'^2} T_s(x, y', t) \right) + 4 \cdot S_2 \cos\left(\frac{2\pi x}{F}\right) \cdot \exp(-a_s \cdot y') \quad (7)$$

where the origin of the  $y'$ -coordinate system lies at the film-substrate interface (Fig. 2). Note that  $F$  is given by

$$F = \frac{\lambda}{2 \cdot \sin(2\theta)} \quad (8)$$

where  $\lambda$  is the laser wavelength and  $\theta$  is the interference angle in radians.  $S'_1$  is given by

$$S'_1 = \frac{(1 - R(h)) \cdot a_m}{(\rho C_p)_m} \cdot \frac{E}{t_p} \quad (9)$$

The boundary condition for continuity of thermal flux at the interface is given by  $k_m \frac{\partial T(x, y, t)}{\partial y} |_{y=h_m} = k_s \frac{\partial T_s(x', y', t)}{\partial y'} |_{y'=0}$ . Initially, the temperature of the system was at ambient and could be expressed by

$T(x, y, t) |_{t=0} = T_s(x', y', t) |_{t=0} = T_o$ . To approximate infinite substrate thickness, we imposed the condition  $T_s(x', y', t) |_{y'=5 \cdot L_{th}} = T_o$  where  $L_{th}$  is the thermal diffusion length of the substrate given by  $L_{th} = \sqrt{t_p \alpha_s}$ . To approximate infinite lateral extent, the period boundary conditions  $T_m(x, y, t) = T_m(x + F, y, t)$  and  $T_s(x', y', t) = T_s(x' + F, y', t)$  were also imposed. In Fig. 4, the calculated behavior of the temperature on the surface of a continuous Co film on Si under laser-interference irradiation is shown. The Co film was 1 nm thick while the interference fringe spacing was 400 nm. In Fig. 4(a) the instantaneous temperature profile along the x-direction is shown at a time of 10 ns into the irradiation and the temperature variation is periodic with the fringe spacing of  $\Lambda = 400 \text{ nm}$ . In Fig. 4(b) the time dependence of the temperature at the fringe maxima and minima is plotted. The phase changes, i.e. melting and resolidification of film and substrate, are visible as distinct slope changes in the curves. From this behavior, the lateral thermal profile as a function of time can be evaluated by subtracting the temperatures at the positions of maxima and minima, as shown in Fig. 4(c). From such numerical calculations, the maximum lateral temperature difference was found to be in the range of  $1 - 10 \text{ K/nm}$  for Co films in the thickness range investigated in this work.

### 3.2 Morphology, length scale and microstructure for energy $E_{Co} \leq E_1 < E_{Si}$

Fig. 5 represents the typical results following patterning in energy regime  $E_1$ . Fig. 5(a) shows a SEM micrograph and its power spectrum (*PS*) following dynamic patterning of a 4 nm Co film deposited at a rate of 1 nm/min with each beam energy of  $150 \text{ mJ/cm}^2$ . The morphology consists of periodically arranged rows of nanoparticles. The rows are regularly arranged with spacing  $L = 400 \text{ nm}$ , which was identical to the interference fringe spacing  $\Lambda$ . This regular arrangement had long-range periodicity as confirmed by the computer generated diffraction spots visible in the *PS*. Also, the direction of the pattern wavevector was identical to the fringe wavevector. The arrangement of the nanoparticles within each row appeared random, as evidenced by the diffuse intensity in the *PS* for directions perpendicular to the diffraction spots. Fig. 5(b) shows a TEM micrograph and corresponding selected area diffraction (SAD) pattern of a dynamically patterned 6 nm Co film deposited at a rate of 1 nm/min. The LRO period is consistent with the fringe spacing of 400 nm. Indexing of the spots and rings of the diffraction pattern indicated that the crystalline phase of the nanostructures could be indexed primarily as Co metal with bulk hcp phase and the metal-rich silicide phase  $\text{Co}_3\text{Si}$ . Table 1 shows the measured spots and rings corresponding to the nanostructures and they are in excellent agreement with the theoretical spacings for bulk hexagonal Co and  $\text{Co}_3\text{Si}$  phases.

Fig. 6 shows the result of dynamic patterning with single beam energy of  $180 \text{ mJ/cm}^2$  and fringe spacing  $\Lambda = 400 \text{ nm}$  for films of thickness ranging from 0.5 nm to 25 nm. The important feature was that the LRO length scale and wavevector direction corresponded to the interference fringe. However, another important result was that as the particle sizes increased and became comparable to the line spacing  $\Lambda$ , an increasing interaction between the lines was visible, as evident for the 15 nm and 25 nm films in Fig. 6(b) and (c) respectively. This interaction led to a decrease in the overall quality of the spatial order, as evident from the decreasing contrast of the diffraction spots in the *PS* for the various thickness. We also observed that the state of the Si surface played a critical role on the observed pattern microstructure. Identical dynamic patterning experiments were performed on Si surfaces treated by an HF-etch to remove the native oxide. Under these conditions we observed that while the patterns still showed the interference fringe length scale,

the morphology was dominated by a reaction-like microstructure. Fig. 7 shows such a reaction-dominated microstructure in contrast to the particle-like morphology of Fig. 5.

### 3.2.1 Mechanism of pattern formation in regime $E_1$

We attribute the pattern formation in regime  $E_1$  to be dominated by mass transport in the liquid phase with contribution from solid state mass transport during the early stages of deposition. This is based on two experimentally observed features: (i) The final observed nanomorphology shows particulate formation only for energies in regime  $E_1$ . We suggest that this is because at some stage of the dynamic patterning the metal film underwent melting; and (ii) As observed by us previously the patterns formed for energies  $< E_1$  consist of diffuse lines with small aspect ratio [24, 25]. Considering that the melt threshold of the Co metal film is highly thickness dependent and increases with decreasing film thickness, as shown in Fig. 3(a), we suggest that during the early stages of deposition and irradiation the film does not melt. Rather, mass transport occurs via surface diffusion and surface self-diffusion of Co leading to the nucleation and growth of metal clusters. Fig. 8 depicts this model, where after early stages of growth the film consists of discrete particles with larger average size in the lower temperature regions of the fringe. Subsequently when the clusters reach a thickness wherein the laser energy can melt it, liquid phase mass transport will be important. This sequence of solid-state transport and liquid transport eventually results in the observed particulate like patterns.

Based on the observations and the above hypothesis, we have identified the possible hydrodynamic flow mechanisms leading to pattern formation based on the time scales of various contributions to liquid motion. One is the non-uniform temperature of the metal liquid arising from the interference pattern that will result in a surface tension gradient hence contributing a thermocapillary component to flow. A second contribution is the Laplace pressure difference arising from the difference in average metal cluster size that determines the morphology during early stages of film growth. We further assume that the clusters are sufficiently large (i.e. of few 10's of nm) such that their melting and liquid flow contributing to pattern formation can be analyzed using a continuum level approach. We can estimate the time scales involved by evaluating the Navier-Stokes equation for incompressible 1-D flow of a liquid flowing in the  $x$ -direction given by:

$$\rho \frac{dv_x}{dt} = -\frac{dp}{dx} + \eta \frac{d^2 v_x}{dy^2} \quad (10)$$

where  $\rho$  is the density of the liquid;  $v_x$  is the  $x$ -component of the liquid velocity;  $\frac{dp}{dx}$  is the pressure gradient in the direction of flow  $x$ ; and  $\eta$  is the dynamic viscosity. Solving for the low Reynolds number case, which is valid for such thin films, the inertial contribution from  $\rho \frac{dv_x}{dt}$  can be neglected (analogous to the steady state condition) and we get on integrating:

$$v_x = \frac{1}{2\eta} \frac{dp}{dx} y^2 + ay + b \quad (11)$$

where  $a$  and  $b$  are constants of integration. Applying the no-slip boundary condition of  $v_x = 0$  at  $y = 0$ , i.e. the liquid-substrate interface, we get  $b = 0$ . The free surface boundary condition at the liquid-vacuum interface requires that the tangential stress gradients cancel out and hence  $\sigma_{xy} = 0$  at  $y = h$ , the

local liquid height. In the interference experiments, the non-uniform heating results in a non-uniform liquid temperature along the plane of the liquid surface  $x$  causing the surface tension to vary with  $x$ . Further, no temperature gradients exist in the vertical  $y$ -direction because of the small film thickness and the large thermal conductivity. Hence the stress balance condition at the surface, which requires that the viscous stress be balanced by the surface tension gradient stress gives:

$$\eta \frac{dv_x}{dy} = \gamma_T \frac{dT}{dx} \text{ at } y = h \quad (12)$$

where the  $LHS$  is the viscous stress;  $\gamma_T$  is rate of change of surface tension with temperature; and  $\frac{dT}{dx}$  is the gradient in liquid surface temperature in the  $x$ -direction. Using eq. 12 in eq. 11 we get:

$$v_x = \frac{1}{2\eta} \frac{dp}{dx} y^2 - \frac{1}{\eta} \frac{dp}{dx} hy + \frac{\gamma_T}{\eta} \frac{dT}{dx} y \quad (13)$$

The effective liquid velocity can be obtained by averaging over the local thickness of the film such that [30]:

$$v_{av} = \frac{1}{R} \int_0^R v_x dy = -\frac{R^2}{3\eta} \frac{dP}{dx} + \frac{R\gamma_T}{2\eta} \frac{dT}{dx} \quad (14)$$

To estimate the time scale of the liquid flow, the form of the pressure gradient must be explicitly introduced. In our experiments, the dynamic patterning process involves the constant deposition of metal with irradiation by the  $9\text{ ns}$  pulses spaced  $20\text{ ms}$  apart. Numerical calculations show that the liquid lifetime ranges from 1 to 10 ns and therefore, each pulse is thermally independent [26]. In addition, the laser-metal interaction time is a small fraction of the deposition time. Therefore, we can simplify the analysis by analyzing the two likely contributions to pattern formation. (i) During the early stages of deposition when the atom clusters are extremely small and the film is discrete, the non-uniform laser heating produces a small surface height variation  $h(x)$  by surface diffusion, as observed by us in previous work [24, 25]. The height variation is manifested as a film morphology that consists of metal nanoclusters of various sizes  $R(x)$ , with the larger clusters in the thicker regions (Fig. 8). In addition, the height variation has the periodicity of the laser fringe  $\Lambda$ . We further assume that the surface-diffusion results in larger clusters in the regions of the interference *minima*, as would be expected for a thermal-gradient assisted diffusion of surface atoms. (ii) The interference-melting of this non-uniform height leads to the eventual observed nanoparticle patterns. To show this, we use the fact that the metal nanoclusters of various radius of curvature  $R(x)$  producing the height variation will contribute a local Laplace pressure given by  $-\gamma(x)K$ , where  $K = \frac{d^2h}{dx^2} = -\frac{1}{R(x)}$  is the local curvature, which is positive for spherical shaped particles. The surface tension is also now a function of film position because of the thermal gradients resulting from the fringe. Therefore the pressure gradient in the  $x$ -direction can be expressed as:

$$\frac{dp}{dx} = -\gamma \frac{dK}{dx} - K \frac{d\gamma}{dx} = -\frac{\gamma(x)}{R^2} \frac{dR}{dx} + \frac{\gamma_T}{R(x)} \frac{dT}{dx} \quad (15)$$

where we have approximated the local curvature to be given by  $K = 1/R(x)$ . The resulting flow

velocity at any position  $x$  can be obtained by using the above equation in eq. 14 giving:

$$v_{av} = \frac{\gamma}{3\eta} \frac{dR}{dx} - \frac{1}{6\eta} \gamma_T \frac{dT}{dx} R \quad (16)$$

where we have approximated the local film height  $h \sim R(x)$ . The first term contributes to the flow a component similar to that found in Ostwald ripening where regions with lower Laplace pressure grow at the expense of regions with higher pressure. The second term  $\gamma_T \frac{dT}{dx}$  is always negative because the surface tension decreases with increasing pressure and therefore contributes a thermocapillary enhancement to the Laplace component of the pressure (1<sup>st</sup> term in Eq. 16). Equation 16 reduces to the classical Marangoni or thermocapillary flow for a flat film when  $\frac{dR}{dx} = 0$  and  $R = h$ . The time scale  $\tau_L$  of liquid motion over the characteristic length scale of the experiment, given by the distance between the fringe maxima to minima (length scale of  $\Lambda/2$ ) can be estimated by noting that  $v_{av} = \frac{\Lambda/2}{\tau_L}$  and so:

$$\tau_L = \frac{\Lambda}{2} \left\{ \frac{1}{\frac{1}{6\eta} |\gamma_T \frac{dT}{dx}| R + \frac{\gamma}{3\eta} \frac{dR}{dx}} \right\} \quad (17)$$

To make an order of magnitude estimate of  $\tau_L$ , we used the following numbers:  $\eta^{Co} = 4.46 \times 10^{-3} Pa-s$ ;  $\gamma^{Co} = 1.88 J/m^2$ ;  $|\gamma_T^{Co}| = 0.5 \times 10^{-3} J/m^2 - K$ ; and the maximum transient thermal gradient in the fringe as estimated from numerical simulations of  $dT/dx \sim 10 K/nm$ . An estimate of  $R$  and the thickness gradient is more difficult. However, we make two approximations: for the value of  $R$  we used the average final deposited film height of  $h_f$  while for  $dR/dx$  we used our previous results [24, 25] which showed that the Co lines resulting from surface diffusion lead to a height approximately 15-20 times that of the final average film thickness  $h_f$  resulting in  $dR/dx \sim 20 \frac{h_f}{\Lambda/2}$ . We find then that the above equation yields two important results: (i) the Marangoni term is small compared to the capillary term. This suggests that the Laplace pressure difference due to difference particle size plays a dominant role and the patterning process is similar to Ostwald ripening, i.e. the larger particles grow at the expense of the smaller ones; and (ii) the expression can be simplified to  $\tau_L = \frac{3\eta\Lambda^2}{80\gamma h_f} \sim 8.89 \times 10^{-5} \frac{\Lambda^2}{h_f}$  which varies inversely as the film thickness. We can then estimate the time scale for liquid motion occurring at any stage when the surface diffusion has established a thickness variation and when the average film thickness is sufficient such that the film melts under the laser pulse process. For instance, if the film melts at a thickness of  $h_f \sim 0.5 nm$  we get a time scale of  $\sim 28 ns$  for a fringe spacing  $\Lambda = 400 nm$ . While this time implies that the patterning cannot occur under one pulse, it is achievable due to the long integrated liquid lifetime over the time scale of the experiment. The typical experiment times ranged from 0.5 minutes to 5 minutes at a repetition rate of 50 Hz. Using an average liquid lifetime of  $\sim 5 ns$  [26], the total integrated liquid lifetime can be considerable because between 1500 to 15000 pulses are incident during the deposition process.. Therefore, even taking into account that during the initial pulses, when mass transport via solid state processes are likely to dominate, a sufficient integrated time is available for liquid phase motion to dominate the pattern formation.

One can estimate whether mass transport via surface diffusion in the solid state can make a substantial contribution to pattern formation throughout the entire experiment. An estimate of the time scale as well as

the efficiency of mass transport for surface diffusion can be made using the theory given by Mullins [31] in which the time scale and flux for mass transport are respectively:

$$\tau_s = \frac{\Lambda R^2}{2 \frac{D_s}{kT} \gamma \Omega \frac{dR}{dx}} \quad (18)$$

$$J_s = -\frac{2D_s \gamma}{kTR^2 \lambda} \Omega \nu \frac{dR}{dx} \quad (19)$$

where,  $D_s$  is the surface self-diffusion coefficient;  $\Omega$  is the atomic volume;  $k$  is Boltzmann's constant; and  $\nu$  is the areal density of surface atoms. From this we can claim that mass transport by the hydrodynamic process will dominate if:

$$\frac{\tau_L}{\tau_s} < 1; \text{ and } \frac{J_L}{J_s} > 1 \quad (20)$$

Using eq. 17 (and neglecting the Marangoni component) and eq. 18 we get at the melting point of Co of  $T = 1768 K$ :

$$\frac{\tau_L}{\tau_s} = \frac{2D_s \Omega \eta}{kTR^2} = 4 \times 10^{-12} \frac{D_s}{R^2} \quad (21)$$

where we have used  $\Omega = 1/\rho_{at}^{Co} = 1.1 \times 10^{-29} m^3/atom$ , where  $\rho_{at}^{Co} = 8.97 \times 10^{28} atoms/m^3$  is the atomic density of Co. Therefore we see that for the liquid process to be faster  $\frac{D_s}{R^2} < 2.5 \times 10^{11} m^2/s$ . Assuming a film thickness  $h_f = R$  of 0.5 nm and using the experimentally observed value for Co diffusivity of  $D_S^{expt} = 0.48 \times 10^{-8} e^{-0.14 ev/kT}$  [32] we see that  $\frac{\tau_L}{\tau_s} \sim 5 \times 10^{-8}$  and therefore the liquid time scale is much shorter. However, the mass transport efficiency, given by the flux, must also be compared. For the liquid flow, the flux in the  $x$ -direction can be expressed as:

$$J_L = -v_{av} \rho_L^{at} \quad (22)$$

where  $\rho_L^{at}$  is the atomic number density in the liquid phase. From eq. 14, eq. 19 and eq. 22 we get that liquid transport dominates when:

$$\frac{J_L}{J_S} = \frac{(\rho_{Co}^{at})^{4/3} kTR^2}{6\eta D_s} \sim \frac{2 \times 10^{14} R^2}{D_s} > 1$$

where we have used the approximation that the liquid and solid atomic densities of Co are comparable, i.e.  $\rho_L^{at} \sim \rho_{Co}^{at}$ . Here also we find that for films of 0.1 nm thickness or larger the flux carried by the liquid is significantly larger than the solid state implying that liquid-based mass transport is most likely responsible for the observed pattern formation.

### 3.3 Morphology, length scale and microstructure for energy $E_2 \geq E_{Si}$

Fig. 9 represents the typical results following patterning in energy regime  $E_2$ . Fig. 9(a) shows an AFM topographic image and its power spectrum ( $PS$ ) following dynamic patterning of a 2 nm Co film deposited at a rate of 1 nm/min with an interference angle of  $42^\circ$ . The direction of the laser interference fringe is marked in the top right corner of the AFM image. A distinctly different nanomorphology is observed for

this regime, as compared to Fig. 5(a). The quantitative differences include: (i) a more elliptical shape of the nanofeatures as compared to the more droplet-like shapes observed in  $E_1$ ; (ii) an ordering length scale different from  $\Lambda$ ; and (iii) a two-dimensionally (2-D) periodic arrangement of the features. The LRO length scale in the direction of the interference wavevector, also seen as diffraction spots in direction  $A$  in the  $PS$ , was estimated to be 240 nm, which is smaller than  $\Lambda = 400\text{ nm}$ . In addition, the features have spatial order along each of the rows, as evident from the 2-D nature of the diffraction pattern in the  $PS$ . The spots visible in direction  $B$  correspond to a feature spacing of  $\sim 522\text{ nm}$ . Fig. 9(b) shows a TEM micrograph and corresponding selected area diffraction (SAD) pattern of a dynamically patterned 2 nm Co film deposited at a rate of 1 nm/min. The general results, i.e. the 2-D form of ordering and an LRO length scale of  $L \neq \Lambda$  are consistent with the AFM image. Indexing of the spots in the diffraction pattern indicated that the crystalline phase of the nanostructures was primarily Cobalt silicide with excellent matching to the Si-rich  $\text{CoSi}_2$  phase. Table 2 shows the measured spot spacings and the theoretical spacings for cubic  $\text{CoSi}_2$ .

Fig. 6 shows the result of dynamic patterning in energy regime  $E_2$  with fringe spacing  $\Lambda = 400\text{ nm}$  for films of thickness of 0.5 nm (deposited at 0.1 nm/min) and 1 nm (deposited at 1 nm/min). The 2-D ordering, as in the 2 nm case of Fig. 9, is clearly evident from the AFM images and the corresponding  $PS$ . Again, like the 2 nm case the LRO visible as spots in direction A, and had spacing  $L < \Lambda$  with values of 232 nm and 233 nm for the 0.5 and 1 nm film respectively. Another feature is that the average LRO spacing in the B direction increased with increased thickness and was estimated to be 172, 474 and 522 nm for the 0.5, 1 and 2 nm film. The average diameter of the features also increased and was 68, 98 and 120 nm for 0.5, 1 and 2 nm films respectively.

### 3.3.1 Mechanism of pattern formation in regime $E_2$

One of the striking results for irradiation in this regime is that pattern formation also occurred on the bare Si substrate surface without any Co deposition. As shown in an exhaustive work by Pedraza et al [18], the rippling of the Si surface is due to melting and the various resulting periodic length scales come from interference of beams scattered along the surface due to surface roughness as well as with surface electromagnetic waves (SEW), a phenomenon that has been widely studied in the past. Further, they also observed that the morphology was a function of the irradiation time and proposed that hydrodynamic instabilities can cause the morphologies. We suggest that our patterns observed in this energy regime come from similar mechanisms. The first evidence is the origin of the observed LRO length scale in the  $A$  direction of approximately  $\sim 232\text{ nm}$ . The general grating wavelength  $\Lambda^g$  resulting from interference between the incident beam with wavevector  $k$  and the scattered beam with wavevector  $k^{sc}$  can be expressed as:

$$\Lambda_{+/-}^g = \frac{2\pi}{k^{sc} \pm k \sin\theta_i} \quad (23)$$

where  $\theta_i$  is the incident angle of the laser light. Depending upon the mechanism of the scattered beam, various grating wavelengths can be observed. In our case, the closest agreement occurs for interference with the beam scattered in reflection for which case  $k^{sc} = kn$ , where  $n$  is the refractive index for Si at 266 nm and is 1.831. Using this we find that  $\Lambda_-^g = 229\text{ nm}$ , which is very close to the observed LRO

visible as diffraction spots in the  $A$  directions of the PS of figures 9 and 10. In addition, we observed an identical length scale on the bare Si surface suggesting that the deposition of Co during the dynamic patterning process played a negligible role in determining the grating spacing. This result is intriguing primarily because the patterned microstructure comprises a Co-silicide phase while the LRO length scale is determined by the Si surface. The second ordering length scale appearing in the PS along direction  $B$  (Fig. 9 and 10), which was perpendicular to the interference fringe direction, cannot be explained by similar surface interference phenomenon because the length scale changes with thickness and/or irradiation time. While further investigations are required to understand this length scale in detail, one possible mechanism is a Rayleigh-like breakup of the elongated liquid region consisting of the Co-Si mixture during the laser melting. It is well known that the classical break-up of a liquid cylinder, driven by minimization of the surface area, leads to preferred wavelengths and typically the wavelength and diameter increase linearly with the cylinder diameter. Qualitatively, one would expect that as the Co concentration is increased the volume of the Co-Si liquid phase will also increase and hence the observed trend of increase in spacing and diameter of the particles in going from the 0.5 to 2 nm film.

## 4 Conclusion

We have investigated the pattern formation resulting from Co film deposition with simultaneous ns pulsed laser interference irradiation of the Si(001) surface as a function of laser energy and film thickness. We found that the  $E$  required to melt the Co film ( $E_{Co}$ ) was lower than the bare Si surface ( $E_{Si}$ ) because of the higher reflectivity of the Si surface and the heat sinking effects of the substrate. Consequently, for energy densities  $E_{Co} < E_1 < E_{Si}$  that preferentially melted the Co film, spatially ordered nanoparticles were formed by capillary-driven transport in the liquid phase. The ordering length scale corresponded to the interference fringe spacing  $\Lambda$  and the microstructure was primarily Co metal and a metal-rich silicide phase. The native oxide layer played an important role in minimizing the Co-Si reaction. For laser energy densities  $E_2 \geq E_{Si}$ , spatially ordered patterns with periodic length scales  $L < \Lambda$  were observed and resulted from interference of an incident laser beam with a beam transmitted into the Si substrate. These nanopatterns showed both one- as well as two-dimensional spatial ordering of the nanostructures. The microstructure in this laser energy regime was dominated by Si-rich silicide phase formation. These results suggest that various nanostructures and microstructures, ranging from nearly pure metal to the silicide can be formed by appropriate choice of the laser energy simultaneous with film growth.

RK acknowledges support by the National Science Foundation through a CAREER grant # DMI-0449258 and is indebted to Prof. R. Sureshkumar for valuable comments on hydrodynamics. The authors would also like to thank Chris Favazza and H.Krishna for confirming some of the experimental results.

## References

- [1] K. Inomata and Y. Saito. Spin-dependent tunneling through layered ferromagnetic nanoparticles. *Appl. Phys. Lett.*, 73:1143–45, 1998.

- [2] J.B. Stahl, M.K. Debe, and P.L. Coleman. Enhanced Bioadsorption characteristics of a uniquely nanostructured thin film. *J. Vac. Sci. Tech. A*, 14:1761–64, 1996.
- [3] R.L. White. The physical boundaries to high-density magnetic recording. *J. Mag. Magn. Mat.*, 209:1–5, 2000.
- [4] C.T. Black, C.B. Murray, R.L. Sandstrom, and S. Sun. Spin-dependent tunneling in self-assembled Co-nanocrystal superlattices. *Science*, 290:1131–34, 2000.
- [5] M. Quinten, A. Leitner, J.R. Krenn, and F.R. Aussenegg. Electromagnetic energy transport via linear chains of silver nanoparticles. *Optics Lett.*, 23(17):1331–33, 1998.
- [6] S. A. Maier, P. G. Kik, H. A. Atwater, S. Meltzer, E. Harel, B. E. Koel, and A . A. G. Requicha. Local detection of electromagnetic energy transport below the diffraction limit in the metal nanoparticle plasmon waveguides. *Nature Materials*, 2:229, 2003.
- [7] S. Fan, M. Chapline, N. Franklin, T. Tombler, A. Cassell, and H. Dai. Self-Oriented Regular Arrays of Carbon Nanotubes and Their Field Emission Properties. *Science*, 283:512–514, 1999.
- [8] J.C. Lodder, M.A.M. Haast, and L. Abelman. Patterned magnetic thin films for ultra high density recording. In G.C.Hadjipannayis, editor, *Proceedings of NATO advanced study Institute on magnetic systems beyond 2000*, pages 117–145. Kluwer Academic Publishers, Dordrecht, Netherlands, 2002.
- [9] D. Bäuerle. Laser-chemical processing: recent developments. *App. Surf. Sci.*, 106:1–10, 1996.
- [10] J.C. Miller and R.F. Haglund, editors. *Laser ablation and desorption*, volume 30 of *Experimental methods in the physical sciences*, chapter 1, 2, 4 & 5. Academic Press, San Diego, 1998.
- [11] D.J. Ehrlich and J.Y. Tsao. A Review of Laser-Microchemical Processing. *J. Vac. Sci. Tech. B*, 1:969–984, 1983.
- [12] M. Birnbaum. Semiconductor Surface Damage Produced by Ruby Lasers. *J. Appl. Phys.*, 36:3688–89, 1965.
- [13] S. R. J. Brueck and D. J. Ehrlich. Stimulated surface-plasma-wave scattering and growth of a periodic structure in laser-photodeposited metal films. *Phys. Rev. Lett.*, 48(24):1678–1681, Jun 1982.
- [14] Harvey E. Cline. Surface rippling induced in thin films by a scanning laser. *J. Appl. Phys.*, 52(1):443–448, 1981.
- [15] N. Arnold, P.B. Kargl, and D. Bauerle. Laser direct writing and instabilities. *Appl. Surf. Sci.*, 86:457, 1995.
- [16] D. Y. Kim, S. K. Tripathy, Lian Li, and J. Kumar. Laser-induced holographic surface relief gratings on nonlinear optical polymer films. *Appl. Phys. Lett.*, 66(10):1166–1168, 1995.

[17] H. Kumagai, M. Ezaki, K. Toyoda, and M. Obara. Periodic submicrometer dot structures on n-GaAs substrates fabricated by laser-induced surface electromagnetic wave etching. *J. Appl. Phys.*, 73:1971, 1993.

[18] A. J. Pedraza, Y. F. Guan, J. D. Fowlkes, and D. A. Smith. Nanostructures produced by ultraviolet laser irradiation of silicon. I. Rippled structures. *J. Vac. Sci. Technol. B*, 22:2823–35, 2004.

[19] a) J. D. Fowlkes Y. F. Guan, A. J. Pedraza. Nanostructures produced by ultraviolet laser irradiation of silicon.II. Nanoprolusions and nanoparticles. *J. Vac. Sci. Technol. B*, 22:2836–43, 2004.

[20] J.W. Matthews. *Epitaxial growth, Part A & B*. Academic Press, New York, 1975.

[21] G. Timp, R.E. Behringer, D.M. Tennant, J.E. Cunningham, M. Prentiss, and K.K. Berggren. Using light as a lens for submicron, neutral-atom lithography. *Phys. Rev. Lett.*, 69:1636–39, 1992.

[22] R.E. Behringer, G. Timp, and V. Natarajan. Using a standing wave atom optical lens for nanometer scale lithography. *Proceedings of Quantum Devices and Circuits*, page 24, 1997.

[23] J.J. McClelland, R.E. Scholten, E.C. Palm, and R.J. Celotta. Laser focused atomic deposition. *Science*, 262:877–880, 1993.

[24] Chi Zhang and Ramki Kalyanaraman. In-situ nanostructured film formation during physical vapor deposition. *App. Phys. Lett.*, 83(23):4827–29, 2003.

[25] Chi Zhang and Ramki Kalyanaraman. In-situ lateral patterning of thin films of various materials deposited by physical vapor deposition. *J. Mat. Res.*, 19(2):595–599, 2004.

[26] J. Trice, D. Thomas, C. Favazza, R. Sureshkumar, and R. Kalyanaraman. Investigation of pulsed laser induced dewetting in nanoscopic metal films: thermal modeling and experiments. submitted *Phys. Rev. B*, 2006.

[27] W. Zhang, C. Zhang, and R. Kalyanaraman. Dynamically ordered thin film nanoclusters. *J. Vac. Sci. Tech. B*, 23:L5–L9, 2005.

[28] E. Matthias, M. Reichling, J. Siegel, O. W. Kading, S. Petzoldt, H. Skurk, P. Bizenberger, and E. Neske. The influence of thermal diffusion on laser ablation of metal films. *Appl. Phys. A*, 58:129–136, 1994.

[29] O. S. Heavens. *Optical properties of thin solid*, pages 76–77. Butterworth Publications, ltd., London, 1955.

[30] L. Kondic. Instabilities in gravity driven flow of thin fluid films. *SIAM Review*, 45:95–115, 2003.

[31] W.W. Mullins. Theory of thermal grooving. *J. Appl. Phys.*, 28:333–339, 1957.

[32] J. J. B. Prasad and K. V. Reddy. Lateral self-diffusion and electromigration in cobalt thin films. *J. Phys. D: Appl. Phys.*, 17:125–133, 1984.

## Figure captions:

1. Schematic of the experimental approach used for *dynamic patterning*. The deposition is performed by electron beam evaporation while the two-beam laser interference irradiation is performed using two p-polarized beams from a Nd:YAG laser operating at 266 nm wavelength and 9 ns pulse width.
2. Schematic illustrating the film-substrate geometry used in the analytical and numerical calculations. The boundary conditions at the various interfaces are indicated for the one beam and 2-beam interference calculations.
3. (a) Plot of the thickness dependent reflectivity of the Co-Si based on the model of Heavens [29]. (b) Plot of laser energy density needed to bring Co-Si system to Si melting temperature expressed in terms of the energy density of a single laser beam and assuming 100% contrast between interfering beams.
4. Typical results of numerical calculations of the laser interference heating of a continuous 1 nm Co film on Si substrate. (a) The temperature profile along the surface x-direction at 10 ns showing the temperature variation is periodic with the fringe spacing of  $\Lambda = 400 \text{ nm}$ . (b) The time dependence of the temperature at the fringe maxima and minima. (c) The lateral thermal profile as a function of time obtained from (b) by subtracting the temperature at any given time.
5. Spatial ordering and microstructure following dynamic patterning at energy  $E_1 < E_{Si}$ . (a) SEM image and power spectrum of the pattern in a 4 nm Co film deposited at 1 nm/min. The nanoparticles are arranged in rows which have long range order with a periodic length scale of 400 nm, which is consistent with the interference length scale  $\Lambda$ . The LRO is visible as diffraction spots in the power spectrum. No ordering is visible for the particles within each row, as evidenced by the diffuse form of the power spectrum in directions perpendicular to the spots. (b) TEM micrograph and corresponding selected area diffraction pattern of a 6 nm Co film deposited at 1 nm/min. The LRO period is consistent with the fringe spacing of 400 nm. Indexing of the spots and rings, indicated by numbers on the diffraction image, suggest the presence of Co metal and a small fraction of the metal-rich silicide phase  $\text{Co}_3\text{Si}$  (Table 1).
6. Pattern morphology imaged in the SEM and corresponding PS following dynamic patterning in energy regime  $E_1$  as a function of film thickness. (a) 0.5 nm film deposited at 0.1 nm/min; (b) 15 nm film deposited at a rate of 1 nm/min; (c) 25 nm film deposited at a rate of 1 nm/min. In all three cases, the LRO length scale (400 nm) and wavevector direction corresponded to the interference fringes. The average particle size increased with increasing film thickness and therefore the nature of the ordering decreased presumably due to coalescence of the large particles across the lines. This decrease in ordering quality is visible from the poorly defined diffraction spots for the 25 nm film. Figures (a) and (b) are from our reference [27]
7. Role of the native oxide layer. SEM micrograph of patterning done in regime  $E_1$  for Co on Si surface following removal of the native oxide. The morphology shows evidence for a strong reaction between

the metal and substrate and is in striking contrast to the result of similar patterning performed on the Si surface with the native oxide layer, as shown in Fig. 5(a).

8. Model for the dynamic patterning process. During early stages of deposition and simultaneous irradiation surface diffusion results in a film morphology described by metal clusters of varying size, with the smaller clusters in the higher temperature regions of the laser interference fringe. The clusters and the overlapping temperature profile due to the interference pattern are shown in the figure. The final pattern results following melting and liquid motion from the smaller clusters to the larger ones.
9. Spatial ordering and microstructure following dynamic patterning at energy  $E_2 > E_{Si}$ . (a) AFM image and power spectrum of the surface nanostructure for a 2 nm Co film deposited at 1 nm/min. The direction of the interference fringe is marked in the top right corner of the AFM image. The surface features with periodicity in the direction consistent with the interference fringe have a periodic spacing length scale of 270 nm, which is not consistent with the interference length scale  $\Lambda = 400 \text{ nm}$ . This period is visible as diffraction spots along direction *A* in the *PS*. In addition, clear LRO is visible for the particles within each row leading to a 2-dimensional periodic structure. This is also evidenced in the power spectrum, with the additional diffraction spots visible along direction *B*. (b) TEM micrograph and corresponding selected area diffraction pattern of the dynamically patterned 2 nm Co film. The 2-D nature of the pattern is clearly visible. Indexing of the visible spots (Table 2) indicates that the most dominant phase is the Si-rich silicide  $\text{CoSi}_2$ .
10. Pattern morphology imaged in the AFM with corresponding *PS* following dynamic patterning in energy regime  $E_2$  as a function of film thickness. The line in the inset of the AFM figures point along the expected 2-beam fringe direction. (a) 0.5 nm film deposited at 0.1 nm/min; (b) 1 nm film deposited at a rate of 1 nm/min. In both cases, a 2-D pattern is visible. Similar to the 2 nm case (Fig. 9) the LRO is visible as spots in the *PS* along direction *A* and has spacing  $L < \Lambda$  of 260 nm and 238 nm for the 0.5 and 1 nm film respectively. This length scale is similar to the 2 nm film of 249 nm. On the other hand, the average feature size increased with increasing film thickness and the LRO indicated by spots along *B* was determined to be 172 and 474 nm respectively, as compared to 522 nm for the 2 nm film.

**Table Captions:**

1. Indexing of diffraction spots and rings for the SAD pattern in Fig 5(b) obtained in regime  $E_1$ . The best matching was obtained for crystalline phases corresponding to the bulk Co hcp phase and the metal rich hexagonal  $\text{Co}_3\text{Si}$  silicide phase.
2. Indexing of diffraction spots and rings for the SAD pattern in Fig 9(b) obtained in regime  $E_2$ . The best matching was obtained for crystalline phases corresponding to the Si-rich cubic  $\text{CoSi}_2$  silicide phase.

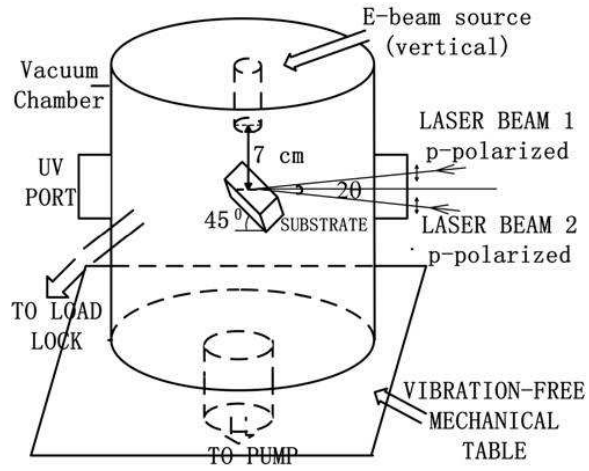


Figure 1: Schematic of the experimental approach used for *dynamic patterning*. The deposition is performed by electron beam evaporation while the two-beam laser interference irradiation is performed using two p-polarized beams from a Nd:YAG laser operating at 266 nm wavelength and 9 ns pulse width.

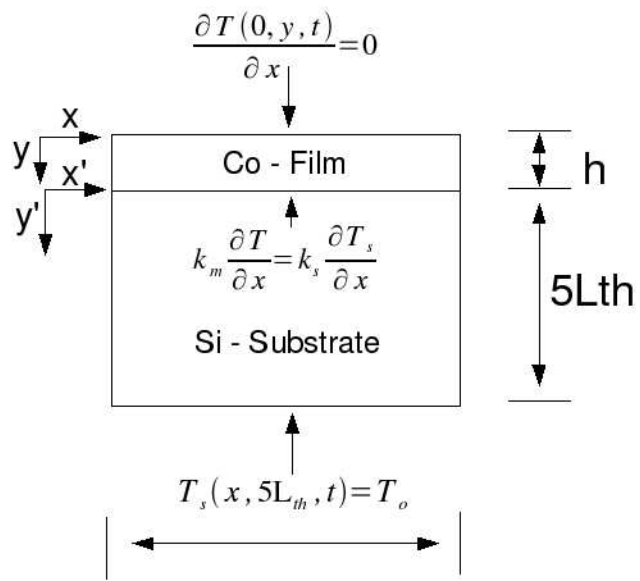


Figure 2: Schematic illustrating the film-substrate geometry used in the analytical and numerical calculations. The boundary conditions at the various interfaces are indicated.

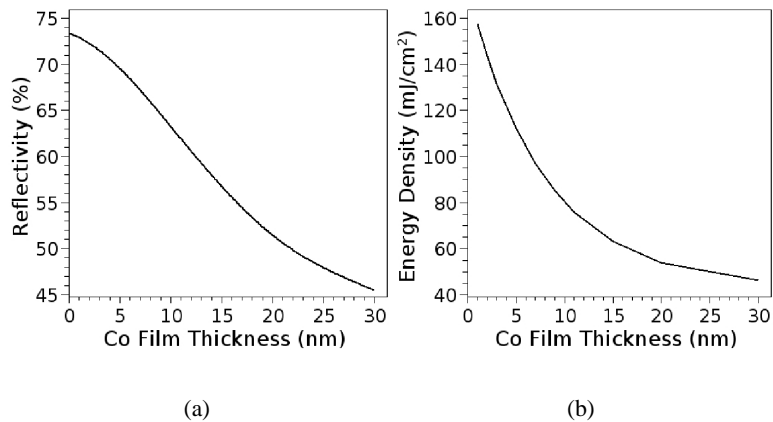
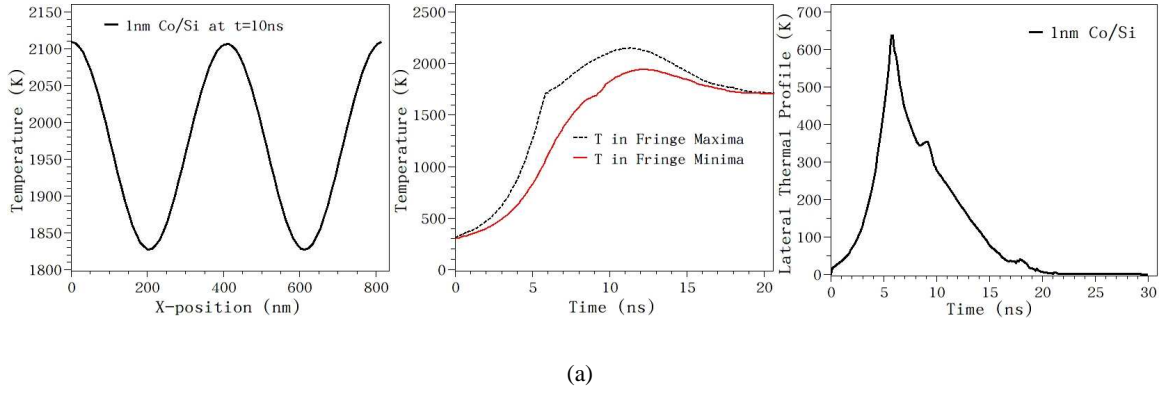


Figure 3: (a) Plot of the thickness dependent reflectivity of the Co-Si based on the model of Heavens [29].  
(b) Plot of laser energy density needed to bring Co-Si system to Si melting temperature expressed in terms of the energy density of a single laser beam and assuming 100% contrast between interfering beams.



(a)

Figure 4: Typical results of numerical calculations of the laser interference heating of a continuous 1 nm Co film on Si substrate. (a) The temperature profile along the surface x-direction at 10 ns showing the temperature variation is periodic with the fringe spacing of  $\Lambda = 400 \text{ nm}$ . (b) The time dependence of the temperature at the fringe maxima and minima. (c) The lateral thermal profile as a function of time obtained from (b) by subtracting the temperature at any given time.

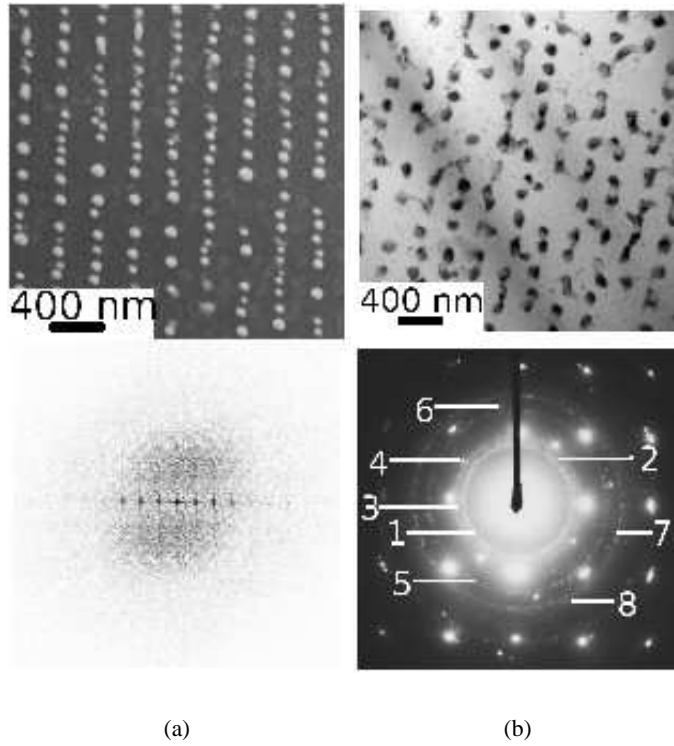


Figure 5: Spatial ordering and microstructure following dynamic patterning at energy  $E_1 < E_{Si}$ . (a) SEM image and power spectrum of the pattern in a 4 nm Co film deposited at 1 nm/min. The nanoparticles are arranged in rows which have long range order with a periodic length scale of 400 nm, which is consistent with the interference length scale  $\Lambda$ . The LRO is visible as diffraction spots in the power spectrum. No ordering is visible for the particles within each row, as evidenced by the diffuse form of the power spectrum in directions perpendicular to the spots. (b) TEM micrograph and corresponding selected area diffraction pattern of a 6 nm Co film deposited at 1 nm/min. The LRO period is consistent with the fringe spacing of 400 nm. Indexing of the spots and rings, indicated by numbers on the diffraction image, suggest the presence of Co metal and a small fraction of the metal-rich silicide phase  $Co_3Si$  (Table 1).

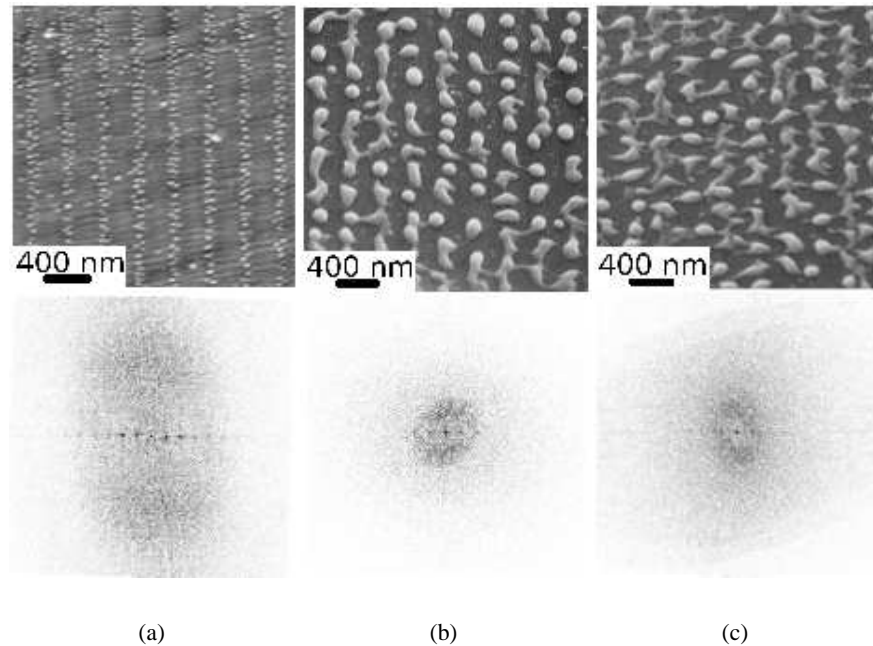


Figure 6: Pattern morphology imaged in the SEM and corresponding *PS* following dynamic patterning in energy regime  $E_1$  as a function of film thickness. (a) 0.5 nm film deposited at 0.1 nm/min; (b) 15 nm film deposited at a rate of 1 nm/min; (c) 25 nm film deposited at a rate of 1 nm/min. In all three cases, the LRO length scale (400 nm) and wavevector direction corresponded to the interference fringes. The average particle size increased with increasing film thickness and therefore the nature of the ordering decreased presumably due to coalescence of the large particles across the lines. This decrease in ordering quality is visible from the poorly defined diffraction spots for the 25 nm film. Figures (a) and (b) are from our reference [27]

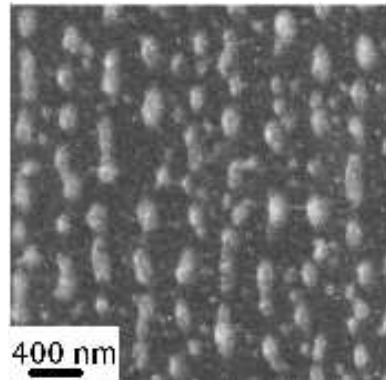


Figure 7: Role of the native oxide layer. SEM micrograph of patterning done in regime  $E_1$  for Co on Si surface following removal of the native oxide. The morphology shows evidence for a strong reaction between the metal and substrate and is in striking contrast to the result of similar patterning performed on the Si surface with the native oxide layer, as shown in Fig. 5(a).

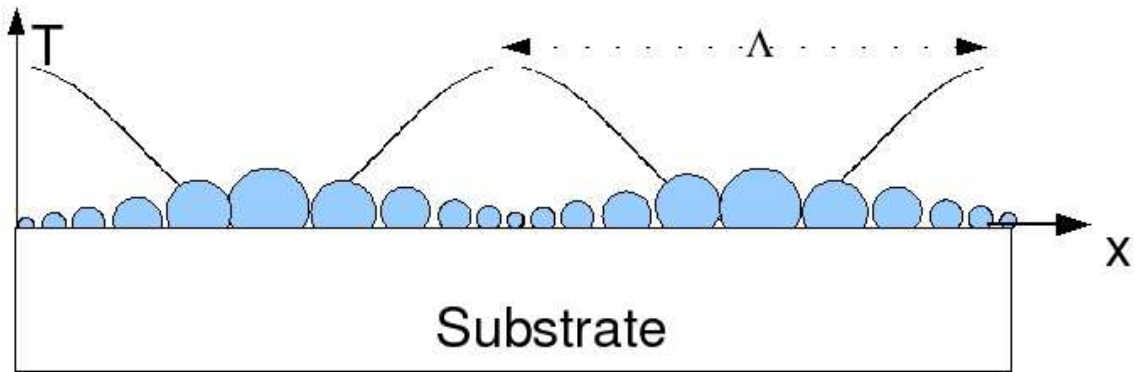


Figure 8: Model for the dynamic patterning process. During early stages of deposition and simultaneous irradiation surface diffusion results in a film morphology described by metal clusters of varying size, with the smaller clusters in the higher temperature regions of the laser interference fringe. The final pattern results following melting and liquid motion from the smaller clusters to the larger ones.

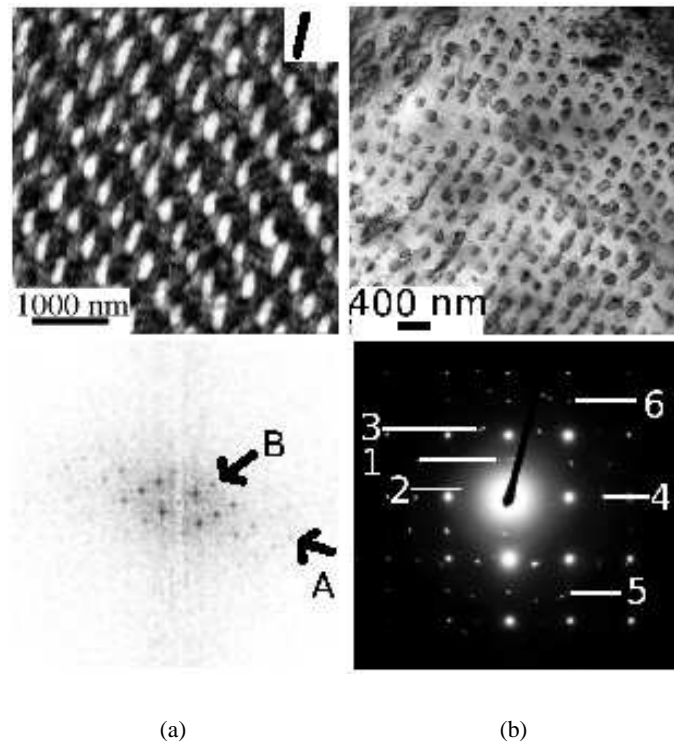


Figure 9: Spatial ordering and microstructure following dynamic patterning at energy  $E_2 > E_{Si}$ . (a) AFM image and power spectrum of the surface nanostructure for a 2 nm Co film deposited at 1 nm/min. The direction of the interference fringe is marked in the top right corner of the AFM image. The surface features with periodicity in the direction consistent with the interference fringe have a periodic spacing length scale of 270 nm, which is not consistent with the interference length scale  $\Lambda = 400\text{ nm}$ . This period is visible as diffraction spots along direction *A* in the *PS*. In addition, clear LRO is visible for the particles within each row leading to a 2-dimensional periodic structure. This is also evidenced in the power spectrum, with the additional diffraction spots visible along direction *B*. (b) TEM micrograph and corresponding selected area diffraction pattern of the dynamically patterned 2 nm Co film. The 2-D nature of the pattern is clearly visible. Indexing of the visible spots (Table 2) indicates that the most dominant phase is the Si-rich silicide  $\text{CoSi}_2$ .

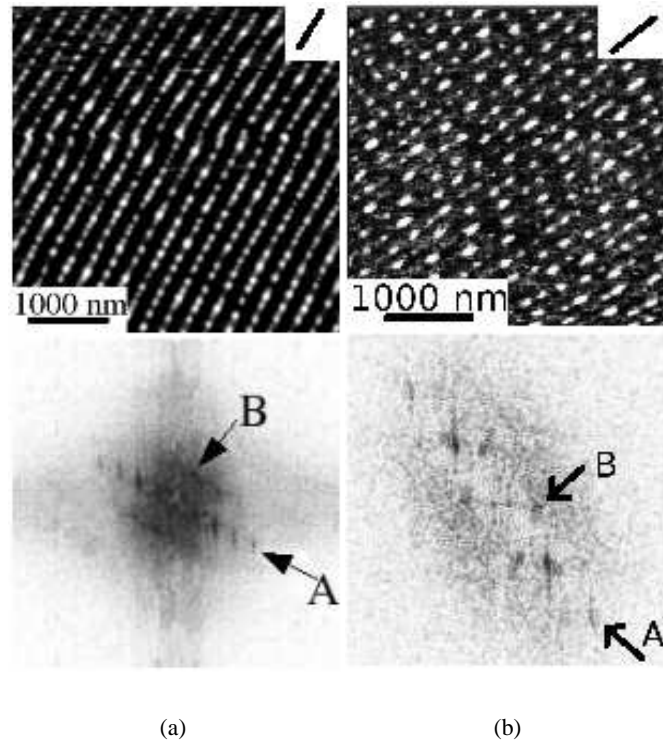


Figure 10: Pattern morphology imaged in the AFM with corresponding *PS* following dynamic patterning in energy regime  $E_2$  as a function of film thickness. The line in the inset of the AFM figures point along the expected 2-beam fringe direction. (a) 0.5 nm film deposited at 0.1 nm/min; (b) 1 nm film deposited at a rate of 1 nm/min. In both cases, a 2-D pattern is visible. Similar to the 2 nm case (Fig. 9) the LRO is visible as spots in the *PS* along direction *A* and has spacing  $L < \Lambda$  of 260 nm and 238 nm for the 0.5 and 1 nm film respectively. This length scale is similar to the 2 nm film of 249 nm. On the other hand, the average feature size increased with increasing film thickness and the LRO indicated by spots along *B* was determined to be 172 and 474 nm respectively, as compared to 522 nm for the 2 nm film.

#	$d^{Expt}(\text{\AA})$	$d(hkl) - Co - hcp\ phase$	$d(hkl) - Co_3Si$
1	$2.41 \pm 0.1$		2.49 (110)
2	$2.23 \pm 0.1$	2.17 (100)	
3	$2.05 \pm 0.1$	2.02 (002)	2.03 (002)
4	$1.91 \pm 0.09$	1.91 (101)	1.9 (201)
5	$1.43 \pm 0.07$	1.48 (102)	
6	$1.33 \pm 0.06$		1.36 (003)
7	$1.25 \pm 0.06$	1.24 (110)	
8	$1.16 \pm 0.06$	1.15 (103)	

Table 1: Indexing of diffraction spots and rings for the SAD pattern in Fig 5(b) obtained in regime  $E_1$ . The best matching was obtained for crystalline phases corresponding to the bulk Co hcp phase and the metal rich hexagonal  $Co_3Si$  silicide phase.

#	$d^{Expt}(\text{\AA})$	$d(hkl) - CoSi_2$
1	3.12	3.1 (111)
2	2.62	2.68 (200)
3	1.62	1.55 (222)
4	1.23	1.23 (331)
5	1.11	1.09 (422)
6	1.06	1.03 (511)

Table 2: Indexing of diffraction spots and rings for the SAD pattern in Fig 9(b) obtained in regime  $E_2$ . The best matching was obtained for crystalline phases corresponding to the Si-rich cubic  $CoSi_2$  silicide phase.